The Astrophysical Journal, 859:15 (12pp), 2018 May 20 https://doi.org/10.3847/1538-4357/aabb56

The Peculiar Radial Distribution of Multiple Populations in the Massive Globular Cluster M80

E. Dalessandro[1], M. Cadelano[1,2], E. Vesperini[3], M. Salaris[4], F. R. Ferraro[1,2], B. Lanzoni[1,2], S. Raso[1,2], J. Hong[3,5], J. J. Webb[3,6], and A. Zocchi[1,2,7]
[1] INAF—Astrophysics and Space Science Observatory Bologna, Via Gobetti 93/3 I-40129 Bologna, Italy; emanuele.dalessandro@oabo.inaf.it
[2] Dipartimento di Fisica e Astronomia, Via Gobetti 93/2 I-40129 Bologna, Italy
[3] Department of Astronomy, Indiana University, Swain West, 727 E. 3rd Street, IN 47405 Bloomington, USA
[4] Astrophysics Research Institute, Liverpool John Moores University, IC2 Liverpool Science Park, 146 Brownlow Hill, Liverpool L3 5RF, UK
[5] Kavli Institute for Astronomy and Astrophysics, Peking University, Yi He Yuan Lu 5, HaiDian District, Beijing 100871, People's Republic of China
[6] Department of Astronomy & Astrophysics, University of Toronto, 50 St. George Street, Toronto, ON M5S 3H4, Canada
[7] European Space Research and Technology Centre, Keplerlaan 1, 2200 AG Noordwijk, The Netherlands
Received 2018 January 31; revised 2018 March 30; accepted 2018 March 30; published 2018 May 17

Abstract

We present a detailed analysis of the radial distribution of light-element multiple populations (LE-MPs) in the massive and dense globular cluster M80, based on a combination of UV and optical *Hubble Space Telescope* data. Surprisingly, we find that first-generation (FG) stars (FG) are significantly more centrally concentrated than extreme second-generation (SG) stars out to $\sim 2.5 r_h$ from the cluster center. To understand the origin of such peculiar behavior, we used a set of *N*-body simulations following the long-term dynamical evolution of LE-MPs. We find that, given the advanced dynamical state of the cluster, the observed difference does not depend on the primordial relative distributions of FG and SG stars. On the contrary, a difference of $\sim$0.05–0.10 $M_{\odot}$ between the average masses of the two subpopulations is needed to account for the observed radial distributions. We argue that such a mass difference might be the result of the higher He abundance of SG stars (of the order of $\Delta Y \sim 0.05$–0.06) with respect to FG stars. Interestingly, we find that a similar He variation is necessary to reproduce the horizontal branch morphology of M80. These results demonstrate that differences in mass among LE-MPs, due to different He content, should be properly taken into account for a correct interpretation of their radial distribution, at least in dynamically evolved systems.

Key words: globular clusters: individual (NGC 6093) – Hertzsprung–Russell and C–M diagrams – techniques: photometric

1. Introduction

Almost all massive (>4–$5 \times 10^4 M_{\odot}$) and relatively old (>2 Gyr) globular clusters (GCs) studied with spectroscopic or photometric observational investigations have been shown to host light-element multiple populations (LE-MPs) characterized by different abundances in a number of light-elements (e.g., C, N, Na, O, He, Al, Mg).

LE-MPs appear to be ubiquitous, as they have been directly observed in Galactic globular clusters (e.g., Gratton et al. 2012, for a review), as well as in external systems such as the Magellanic Clouds and the Fornax dwarf galaxy (Mucciarelli et al. 2008; Larsen et al. 2014; Dalessandro et al. 2016). Moreover, their presence has been indirectly constrained in the GC systems of M31 and M87 (Chung et al. 2011; Schiavon et al. 2013).

LE-MPs manifest themselves in very different ways in the color–magnitude diagrams (CMDs) when appropriate filter combinations are used. In particular, (near-)UV filters are efficient in separating LE-MPs in CMDs, as variations of the OH, CN, and CH molecular bands have particularly strong effects in the spectral range $3000 < \lambda$ (Å) < 4000 (Sbordone et al. 2011). Indeed, recent and extensive UV *Hubble Space Telescope* observations, like *T*he UV Legacy Survey of Galactic Globular Clusters (Piotto et al. 2015), have allowed a significant leap in our understanding of LE-MPs and their census in GCs. These observations have shown that GCs can host from two up to seven (photometrically distinct) stellar populations and their relative number ratios can vary from one cluster to another with some dependence on cluster mass (Piotto et al. 2015; Milone et al. 2017).

CN-weak, Na-poor stars are commonly referred to as first-generation/populations (FG) and the CN-strong, Na-rich ones are referred to as second-generation/population (SG). Both are believed to have formed during the very early epoch of GC formation and evolution ($\sim$10–100 Myr—Decressin et al. 2007; D'Ercole et al. 2008; de Mink et al. 2009; Denissenkov & Hartwick 2014). However, no consensus has yet been reached on the multiple-population formation history and we still lack a complete self-consistent explanation of the physical processes at the basis of LE-MP and GC formation.

The key to shedding new light on the MP phenomenon is a comprehensive description of their properties by means of state-of-the-art photometry and spectroscopy, combined with an in-depth characterization of their kinematics. Indeed, a number of theoretical studies have predicted that SG and FG stars would form with different initial spatial and kinematical properties (see e.g., D'Ercole et al. 2008) and some clusters could still retain some memory of these primordial differences (see, e.g., Mastrobuono-Battisti & Perets 2013; Vesperini et al. 2013; Hénault-Brunet et al. 2015).

Observational evidence of kinematic differences between FG and SG stars have been recently found in a few clusters (see Richer et al. 2013; Bellini et al. 2015; Cordero et al. 2017), based on proper motions and radial velocities. In addition, SG stars are generally observed to be more centrally concentrated than FG stars (e.g., Bellini et al. 2015; Dalessandro et al. 2016;

Massari et al. 2016, for recent results), while only in a few clusters, namely NGC 6362 (Dalessandro et al. 2014), NGC 6121, NGC 6752 (Nardiello et al. 2015), and M13 (Savino et al. 2018), do FG and SG stars show the same radial distribution. This lack of difference in the radial distributions is typically interpreted as the result of a cluster's advanced dynamical evolution (Vesperini et al. 2013; see also Miholics et al. 2015) and significant mass-loss due to both two-body relaxation and interaction with the host galaxy.

In this context, the case of M15 is very peculiar (Larsen et al. 2015): FG stars are found to be more centrally concentrated than the SGs stars out to the cluster's half-light radius,[8] while beyond this radius the trend is inverted and the SG population is more concentrated than the FG one (Lardo et al. 2011). However, this result has been recently questioned by Nardiello et al. (2018).

Following on the variety of results revealed by these observational studies and the possible constraints they provide for our understanding of GC formation and dynamical evolution, in this paper we report on the radial distribution of LE-MPs in the massive and dense GC NGC 6093 (M80). The presence and classification of LE-MPs in M80 have been previously discussed by Piotto et al. (2015) and Milone et al. (2017) and we refer the readers to these papers for further details. Based on both the number and radial distribution of its blue straggler star (BSS) population, Ferraro et al. (2012) classified M80 as a *dynamical old* (i.e., dynamically evolved) stellar system (see also Lanzoni et al. 2016). Indeed, it has been suggested to be in a transient dynamical state during which stellar interactions are delaying the core-collapse process, leading to the observed very high fraction of BSSs (Ferraro et al. 1999).

The paper is structured as follows. In Section 2 the adopted data sets and data-reduction procedures are described. Section 3 reports on the LE-MP selection in the CMD and Section 4 provides their radial distributions. In Section 5 we present the results of a set of *N*-body models aimed at providing some theoretical guidance on the interpretation of our observational results. In Section 6 we analyze the horizontal branch (HB) morphology of the cluster to constrain the maximum He variation among LE-MPs. In Section 7 we summarize the main results.

2. Observations and Data Analysis

To study the radial distribution of M80, we used a combination of *HST* WFC3/UVIS images acquired in the *F*275*W*, *F*336*W*, and *F*438*W* bands through proposal GO-12605 (PI: Piotto), data obtained with the ACS/WFC in the *F*606*W* and *F*814*W* bands (GO-10775, PI: Sarajedini), and one ACS/HRC image obtained in the *F*250*W* band acquired through proposal GO-10183 (PI: Knigge; see Figure 1). Details about each data set are reported in Table 1. Appropriate dither patterns of tens of arcseconds have been adopted for each pointing of the WFC3/UVIS and ACS/WFC data sets in order to fill the inter-chip gaps and avoid spurious effects due to bad pixels.

For WFC3/UVIS and ACS/WFC samples we used images processed, flat-fielded, bias-subtracted, and corrected for charge transfer efficiency (CTE) by the standard *HST* pipeline (flc images). The most updated pixel-area-maps (PAM images) were applied independently to each chip and image. For the ACS/HRC photometry, we used the flat-fielded, bias-subtracted, CTE-corrected, and cosmic-ray-rejected image produced by the standard *HST* pipeline (crj image).

Table 1
Summary of the *HST* Data Sets Used in This Work

Instrument	Filter	t_{exp} (s)	Proposal ID/PI
ACS/HRC	*F*250*W*	1×2348	GO-10183/Knigge
ACS/WFC	*F*606*W*	$4 \times 603 + 1 \times 60$	GO-10775/Sarajedini
	*F*814*W*	4×60	
WFC3/UVIS	*F*275*W*	10×855	GO-12605/Piotto
	*F*336*W*	5×657	
	*F*438*W*	5×85	
WFPC2	*F*160*BW*	4×900	GO-5903/Ferraro
	*F*336*W*	4×600	
	*F*555*W*	$4 \times 23 + 2 \times 2$	

A photometric analysis was performed independently on each chip using DAOPHOT IV (Stetson 1987). Tens of bright and isolated stars were selected in each frame to model the point-spread-function. For the following analysis, we took advantage of the reduced crowding conditions at UV wavelengths using the so-called "UV-route" approach, which is particularly effective for very dense systems like M80 (see for example Ferraro et al. 1998, 2003; Dalessandro et al. 2008, 2009; Raso et al. 2017). Briefly, a first star list was obtained for each image by independently fitting star-like sources above the 5σ level from the local background. Starting from these preliminary catalogs, we then created two UV master-lists. For the most crowded innermost regions, we created a master list using stars detected in the HRC *F*250*W* image, which provides a better sampling than the WFC3 and helps to properly resolve the central regions. In the WFC3 field of view (FOV) complementary to HRC, the master list was obtained using stars detected in at least half of the *F*275*W* images. At the corresponding positions of stars in the combined WFC3+HRC master-lists, a fit was forced in all the available images using DAOPHOT/ALLFRAME (Stetson 1994). For each star thus recovered, multiple magnitude estimates obtained in each chip were homogenized using DAOMATCH and DAOMASTER, and their weighted mean and standard deviation were finally adopted as the star magnitude and photometric error.

Instrumental magnitudes were reported to the VEGAMAG photometric system using the equations and zero-points reported in the dedicated *HST* web pages.

Using the *F*606*W* and *F*814*W* magnitudes and following the approach described in Milone et al. (2012), we estimated the differential reddening within the WFC3/UVIS FOV. Briefly, we rotated the optical CMD onto a photometric reference frame where the abscissa is parallel to the reddening vector. In this reference frame we then defined a fiducial line along the brighter portion of the MS and calculated the distance (d_{redd}) from it along the reddening direction of stars in that magnitude range, which were used as reference stars. For each star in our catalog we computed the average value of d_{redd} of the 30 closest reference stars, which was then used to derive the reddening variation to associate with that star. We found a maximum variation $\Delta(E(B-V)) \sim 0.045$ mag within the

[8] A similar behavior has been suggested by Lim et al. 2016 for NGC362 and NGC6723. However these results are based on ground-based photometry, which may suffer of severe incompleteness in the innermost and dense region of the clusters.

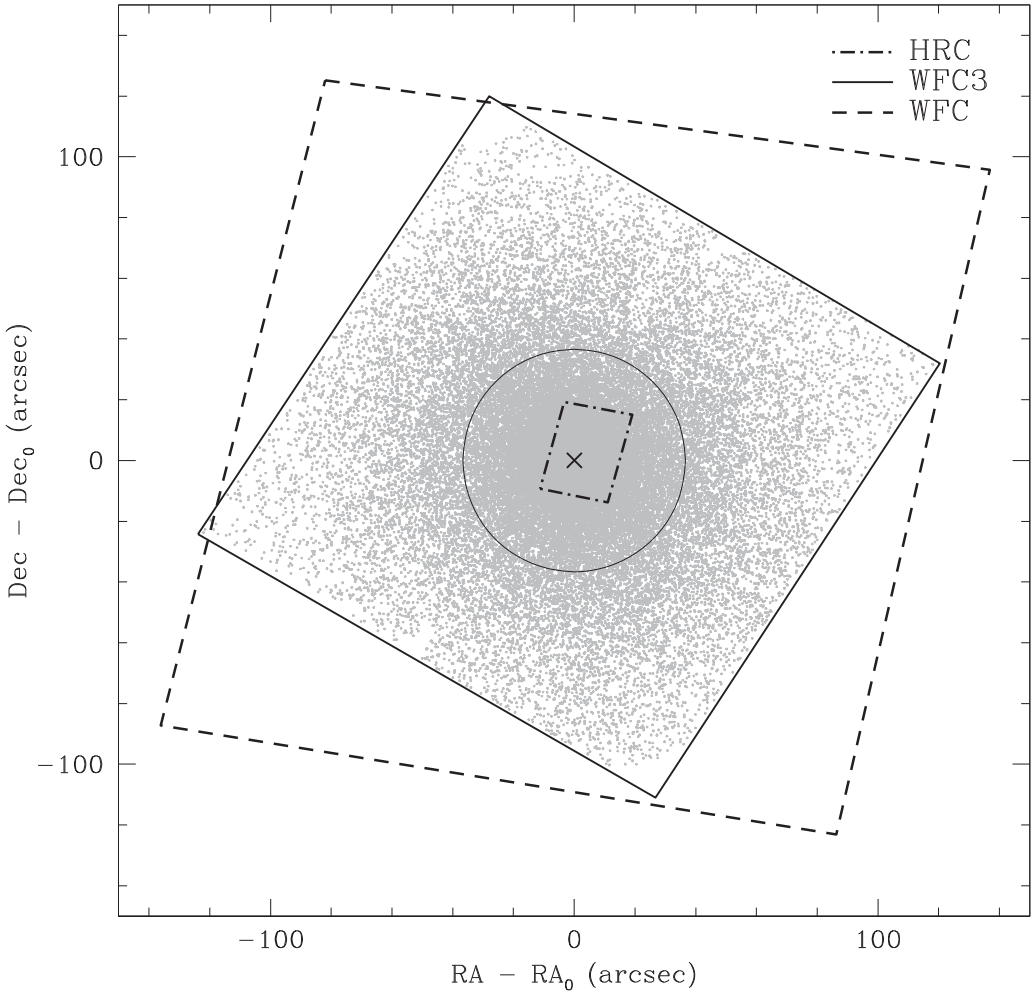

Figure 1. Map of the *HST* database used for the radial distribution analysis of the LE-MPs with respect to the position of $C_{\rm grav}$ indicated with the cross.

entire FOV. The following analysis is based on differential-reddening-corrected magnitudes.

Instrumental coordinates were reported onto the absolute system (α, δ) using the stars in common with the ACS Survey of Galactic Globular Clusters catalog[9] as secondary astrometric standards and the cross-correlation software CataXcorr.

The resulting (m_{F275W}, $m_{F275W} - m_{F438W}$) CMD for stars in the WFC3 FOV is shown in Figure 2. The CMD shows clearly the presence of a well-extended and multi-modal HB (e.g., Ferraro et al. 1998; Dalessandro et al. 2011b) and the presence of large populations of BSSs (Ferraro et al. 2003), depicting an almost vertical sequence extending for about 2 mag in *F*275*W*.

For the analysis of the HB, we used the *HST* WFPC2 catalog (see details about the data set in Table 1) published by Ferraro et al. (1998). The present analysis magnitudes were reported to the VEGAMAG photometric system and corrected for CTE by means of the prescription by Dolphin (2000) and updated equations listed on Dolphin's website.[10] We note that the adoption of the *F*160*BW* far-UV band and the use of the (m_{F160BW}, $m_{F160BW} - m_{F555W}$) CMD are key for clusters with an extended HB, such as M80. In fact, in this diagram the hottest HB stars are the most luminous and lie along almost horizontal sequences whose luminosity is very sensitive to the initial Y abundance, irrespective of the precise value of the stellar mass.

3. Multiple Populations along the Red Giant Branch

Figure 3 (left panel) shows the (m_{F336W}, $C_{275,336,438}$) pseudo-color diagram of M80, where $C_{275,336,438} = ((m_{F275W} - m_{F336W})–(m_{F336W} - m_{F438W}))$. This UV color combination has been used to characterize the LE-MP properties in a large sample of GCs within The HST UV Legacy Survey of Globular Clusters (Piotto et al. 2015; Milone et al. 2017). The combination efficiently highlights the presence of LE-MPs, since it traces simultaneously the strength of the OH, NH, and CH molecular bands. We verticalized the distribution of RGB stars in the magnitude range $17.7 < m_{F336} < 19.4$ in the (m_{F336W}, $C_{275,336,438}$) diagram with respect to two fiducial lines at the bluest and reddest color edges of the RGB (left panel of Figure 3), which have been drawn to include the bulk of RGB stars in the considered magnitude interval. The derived verticalized color distribution ($\Delta_{C_{275,336,438}}$) appears to show three main components (middle panel of Figure 3), which we fit with Gaussian Mixture Models. The result of the fit is shown in the middle panel of Figure 3. Three components can be identified that we classified as FG (red), SG_{INT} (intermediate SG—green), and SG_{EXT} (extreme SG—blue) for increasing values of $\Delta_{C_{275,336,438}}$, as the RGB is populated by stars increasingly enhanced in *N* moving from red to

[9] The catalog is available online at https://www.astro.ufl.edu/~ata/public_hstgc/databases.html.
[10] http://americano.dolphinsim.com/wfpc2_calib/

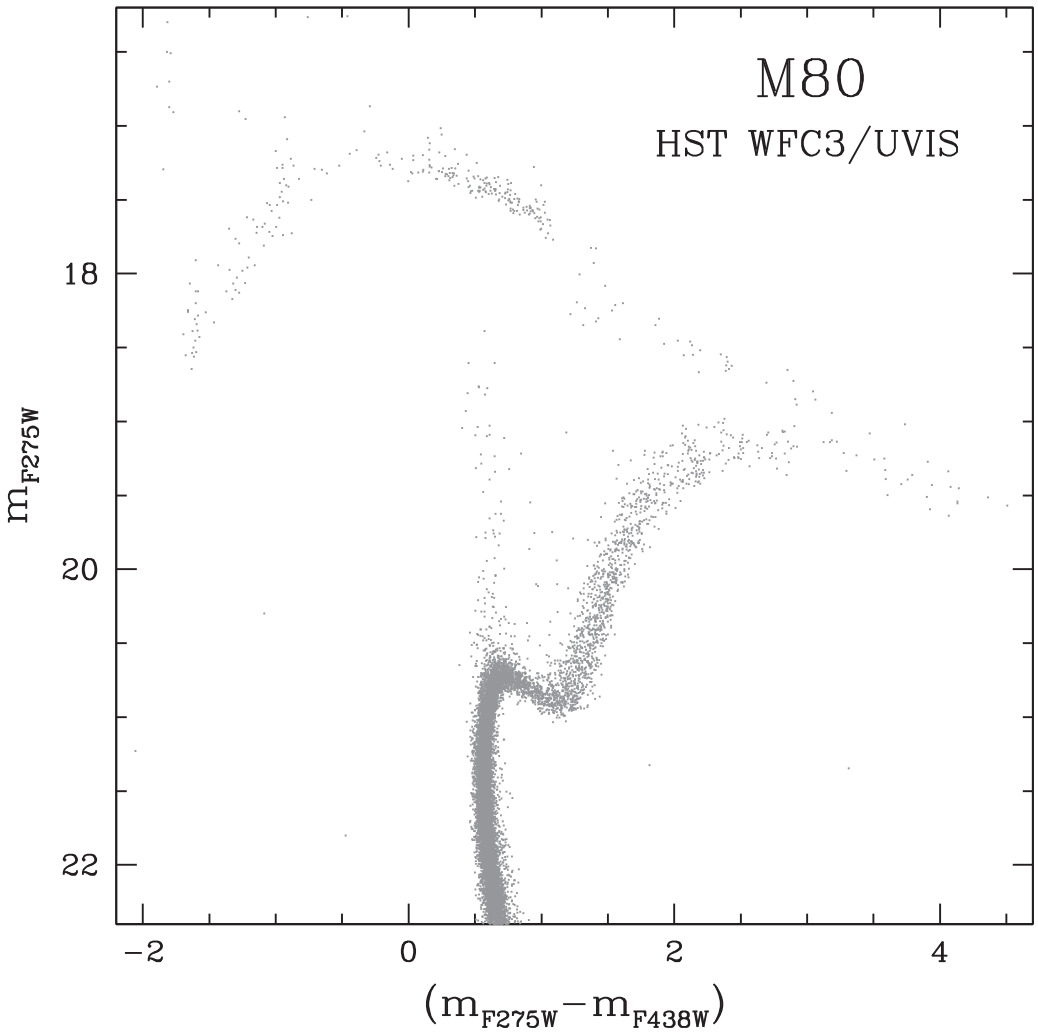

Figure 2. (m_{F275W}, $m_{F275W} - m_{F438W}$) CMD of the stars in the HRC-WFC3 field of view.

blue colors. From the areas under the Gaussian functions, we computed the number ratios among different subpopulations. In particular, we found that $N_{FG}/N_{TOT} = 0.395 \pm 0.023$ (where N_{FG} is the number of FG stars and N_{TOT} the total number of stars selected along the RGB), which is compatible within the errors with the results obtained by Milone et al. (2017) ($N_{FG}/N_{TOT} = 0.351 \pm 0.029$).

Because of the combination of intrinsic color spreads and photometric errors, some degree of overlap is present among the selected subpopulations. To minimize possible contamination among them, in the analysis described in the next sections we will use only stars with a probability $P > 85\%$ of belonging to a given population.

The right panel of Figure 3 shows the so-called "chromosome map" ($\Delta_{275,814}$, $\Delta_{C_{275,336,438}}$). $\Delta_{275,814}$ was obtained by verticalizing the distribution of RGB stars in the (m_{F814W}, $m_{F275W} - m_{F814W}$) CMD with respect to the fiducial lines at the blue and red edges of the RGB. The three subsamples that our analysis is focused on are clearly separated in this diagram.

4. Radial Distribution of Multiple Populations

To study the radial distribution of the LE-MPs of M80, we first derived the center of the cluster (C_{grav}). C_{grav} was determined using an iterative procedure that averages the positions α and δ of stars in a defined magnitude range and lying within a given distance from a first-guess center. At each iteration, star distances are recalculated with respect to the center obtained in the previous iteration until convergence is reached (see, for example, Dalessandro et al. 2013; Cadelano et al. 2017 for more details). We used as a starting guess center the one found by Goldsbury et al. (2010). To avoid spurious and incompleteness effects, we performed various measures of C_{grav} using stars in different magnitude intervals with lower limits in the range $20.9 < m_{F275W} < 21.3$ and distance (d) from the cluster guess center in the range $0'' < d < 30''$–$40''$. The resulting C_{grav} is the average of all these measures, and it is located at ($\alpha = 16^h17^m2\overset{s}{.}481$, $\delta = -22°58'34\overset{''}{.}098$), with an uncertainty of about $0\overset{''}{.}17$. The newly determined center is located at $\sim 1''$ from that obtained by Goldsbury et al. (2010).

We analyzed the radial distributions of FG, SG_{INT}, and SG_{EXT} stars with respect to C_{grav} within the entire WFC3 FOV. The WFC3 FOV extends out to $\sim 2.5 \times r_h$ (where r_h is the half-light radius—$r_h = 36\overset{''}{.}6$; Harris 1996, 2010 edition) and samples $\sim$80% of the total light of the cluster.

Figure 4 shows that the cumulative radial distributions of the three subpopulations are significantly different. Surprisingly, we find that FG stars are more centrally concentrated than the other two sub-groups with the largest difference with SG_{EXT}.

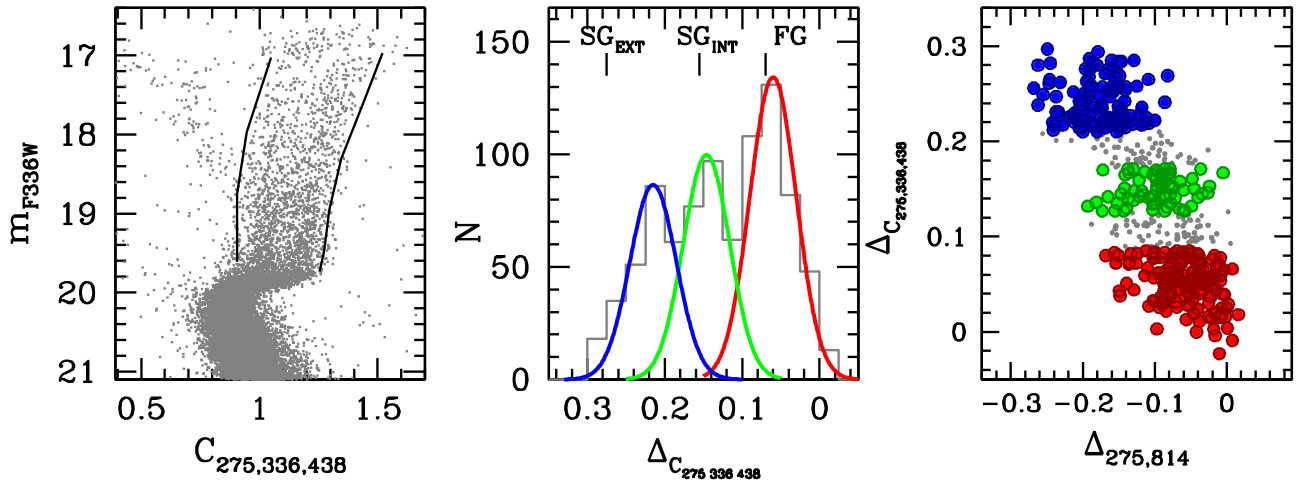

Figure 3. Left panel: (m_{F336W}, $C_{275,336,438}$) pseudo-color diagram of M80. The middle panel shows the $\Delta_{C_{275,336,438}}$ distribution of RGB stars in the magnitude range $17.7 < m_{F336} < 19.4$. Three main components can be identified (see Section 3) that we defined as FG, SG_{INT}, and SG_{EXT}, in red, green, and blue, respectively. Right panel: ($\Delta_{275,814}$, $\Delta_{C_{275,336,438}}$) color–color diagrams of the selected LE-MPs. The colored points represent stars with $P > 85\%$ that belong to one of the three populations.

According to the K-S test, the probability that the FG and SG_{EXT} are extracted from the same parent population is $P \sim 10^{-7}$, while $P \sim 3 \times 10^{-3}$ for FG and SG_{INT} stars. This result is qualitatively similar to what was found in M15 by Larsen et al. (2015, but see Nardiello et al. 2018 for a recent analysis of M15 in which the trend found by Larsen et al. is not confirmed) and it is unexpected in the context of the theories of formation and dynamical evolution of LE-MPs that are available so far.

In the lower panels of Figure 4 the variations of the $N_{FG}/N_{SG_{EXT}}$ and $N_{FG}/N_{SG_{INT}}$ ratios as a function of the distance from C_{grav} are also shown. FG stars are ∼2 and ∼1.5 times more numerous than SG_{EXT} and SG_{INT} stars, respectively, in the innermost regions (∼30″), then the $N_{FG}/N_{SG_{EXT}}$ ratio monotonically decreases reaching a minimum value of ∼0.6, while the $N_{FG}/N_{SG_{INT}}$ ratio seems to have (with moderate significance) a bimodal distribution that reaches a minimum value ($N_{FG}/N_{SG_{INT}} \sim 0.8$) at $d \sim 50''$ and then again outward.

In order to verify the effect of photometric incompleteness on the radial distributions shown in Figure 4, we performed a large number of artificial star experiments following the approach described in Dalessandro et al. (2011a, see also Dalessandro et al. 2015). We found that the three subsamples have photometric completeness $C > 95\%$ in the entire area sampled by our analysis, therefore their radial distributions are virtually unaffected by completeness radial variation effects.

It has been shown that the difference in segregation between different subpopulations can be quantitatively estimated by using the parameter A^+. It was first introduced by Alessandrini et al. (2016, see also Lanzoni et al. 2016) as a mass-segregation indicator for BSSs and it is simply defined as the area enclosed between the cumulative radial distributions of two samples of stars. A^+ has the advantage of not requiring binning of data and allowing an easy and direct comparison among different clusters.

Here we have used the cumulative radial distribution of SG_{EXT} stars as a reference and we have adopted the following definition of A^+:

$$A^+(x) = \int_{x_{min}}^{x} \phi_{FG}(x') - \phi_{SG_{EXT}}(x')dx', \quad (1)$$

where $\phi_{POP}(x)$ is the cumulative radial distribution, $x = (d/d_{max})$ and d_{max} is the maximum distance (expressed in units of r_h) within which A^+ is calculated. With this definition star distances are always comprised in the range 0–1 and a more segregated FG subpopulation leads to positive $A+$ values. Taking advantage of the wide area coverage, we have explored the radial variation of $A+$ by measuring it for three distances: 1.0, 1.5, and 2.0 r_h from C_{grav} (Figure 5). With these prescriptions, we obtain $A^+(1r_h) = 0.02 \pm 0.02$, $A^+(1.5r_h) = 0.08 \pm 0.02$, and $A^+(2.0r_h) = 0.10 \pm 0.01$ when FG and SG_{EXT} subpopulations are considered and $A^+(1r_h) = 0.0 \pm 0.02$, $A^+(1.5r_h) = 0.03 \pm 0.02$, and $A^+(2.0r_h) = 0.04 \pm 0.02$ for FG and SG_{INT} stars. Uncertainties in A^+ have been estimated by applying a jackknife bootstrapping technique (Lupton 1993). $A+$ is recomputed by leaving out one different star from the two considered samples each time. In this way, given a sample of N stars, we end up with N estimates of A^+ computed on samples of $N-1$ stars. The uncertainty on A^+ is therefore $\sigma_{A^+} = \sqrt{N-1} \times \sigma_{sub}$, where σ_{sub} is the standard deviation of the A^+ distribution derived from N subsamples.

5. *N*-body Simulations

To understand to what extent the observational results presented in the previous sections represent an anomaly in the context of the current theoretical models for the formation and evolution of LE-MPs, we have explored the evolution of the spatial distribution of FG and SG stars in two sets of *N*-body simulations following the long-term evolution of the structural properties of multiple-population clusters.

Our simulations start with 50,000 stars equally split between FG and SG stars and have been run using the GPU-accelerated version of the code NBODY6 (Aarseth 2003; Nitadori & Aarseth 2012). Both populations follow the spatial distribution of a King (1966) model with central dimensionless potential equal to $W_0 = 7$, but different values of r_h. In particular, we have explored the evolution of two systems: one in which the SG population's r_h (r_h^{SG}) is about 5 times smaller than r_h^{FG} and one in which r_h^{SG} is about 10 times smaller than r_h^{FG}. The stellar masses are assigned assuming a Kroupa (2001) initial mass function evolved to an age of 11.5 Gyr (the software McLuster —Küpper et al. 2011—has been used to setup the initial conditions). The cluster is tidally limited and assumed to move on a circular orbit in the external potential of a host galaxy modeled as a point mass. As a cluster evolves, it loses mass due

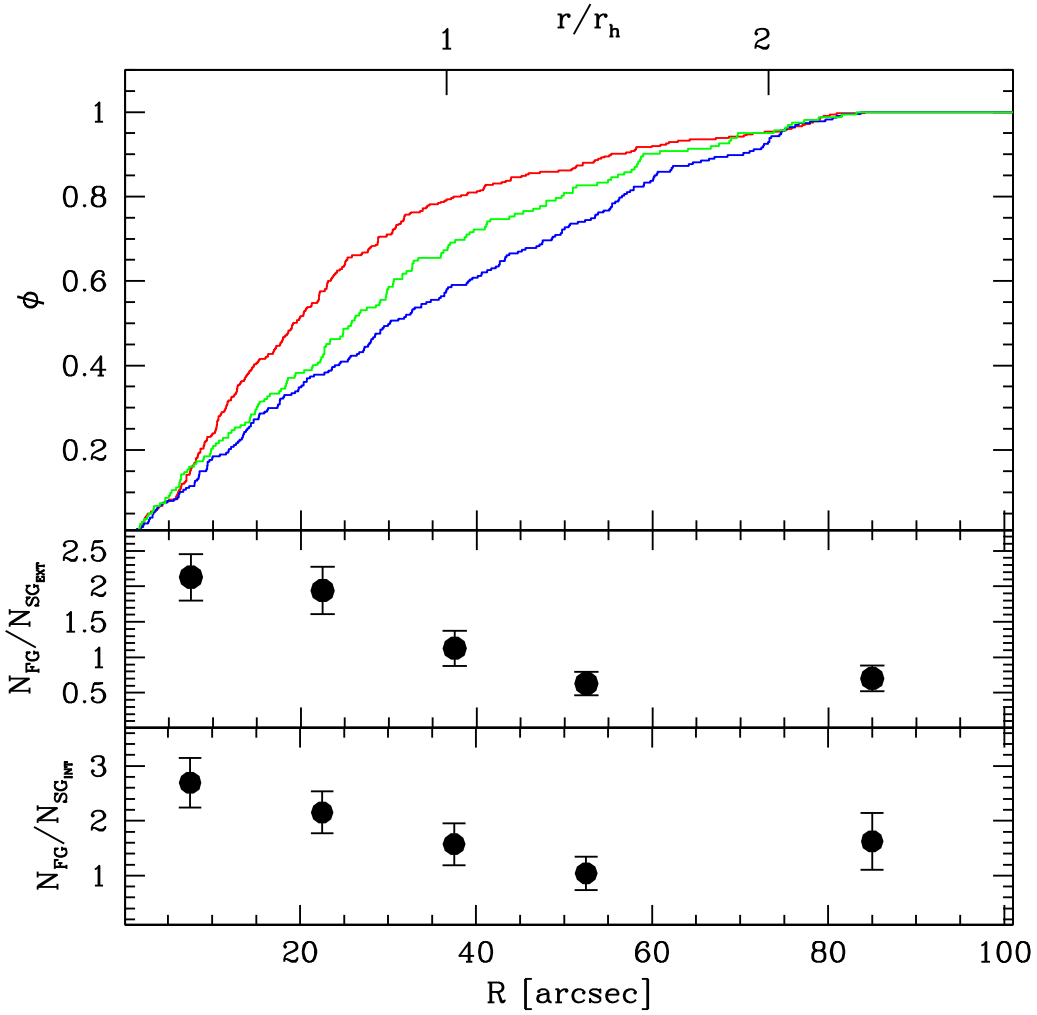

Figure 4. Upper panel: cumulative radial distribution of FG (red), SG_{INT} (green), and SG_{EXT} (blue) stars selected as detailed in Section 3. Lower panels: $N_{FG}/N_{SG_{INT}}$ and $N_{FG}/N_{SG_{EXT}}$ as a function of the distance from the cluster center.

to the combined effects of two-body relaxation and tidal truncation.

We emphasize that the simulations presented here are still simplified and not tailored to provide specific detailed models for M80. Our goal is to illustrate the general evolution of the spatial distributions of FG and SG stars using the A^+ parameter and provide a quantitative measure of the dynamical significance of the effect found in our observational analysis.

In panels (a) and (b) of Figure 6 we show the time evolution of the $A+$ parameter calculated for FG and SG stars with masses $M_{FG} = M_{SG}$ between $0.80\,M_\odot$ and $0.85\,M_\odot$ (as appropriate for RGB stars in an old GC). Time is expressed in units of the instantaneous half-mass relaxation time, t_{rh}. The $A+$ parameter is determined within three projected distances from the center: 1, 1.5, and 2 r_h (dark turquoise, pink, and blue curves, respectively), with r_h being the half-mass–radius.

The systems start with the SG stars concentrated in the cluster's innermost regions, which, considering the definition of A^+ in Section 4, corresponds to negative values of A^+. Panel (a) shows the results for simulations starting with $r_h^{FG} = 5 \times r_h^{SG}$, while panel (b) shows the results for $r_h^{FG} = 10 \times r_h^{SG}$. As the systems evolve and the two populations gradually mix, A^+ increases and evolves toward the value of A^+ corresponding to a mixed cluster ($A^+ = 0$).

It is interesting to note that in our simulations A^+ can reach positive values for dynamically old and mixed systems (at, approximately, $t/t_{rh} > 5$–10). However, we stress that they should not be interpreted as real inversions of the radial distribution, but only as small fluctuations not corresponding to any secular evolution.

We compare our N-body simulations with the observed values of A^+ (gray symbols in Figure 6) by focusing now on the comparison between FG and SG_{EXT}, as they show the most discrepant and significant behavior. For simplicity, in the following we will refer to them as FG and SG, respectively. Clearly, observations appear to deviate significantly from the range of values spanned by A^+ in our simulations when equal mass FG and SG are assumed and they are not compatible with the expected fluctuations. This suggests that the interpretation of the radial distribution of LE-MPs in M80 requires some additional dynamical ingredient.

First, we note that even if we assumed that FG stars formed more concentrated than SG stars, the two subpopulations would be mixed for a cluster with the dynamical age of M80 ($t/t_{rh} \sim 20$). No matter what the details of the formation history of the cluster are and independently of which population was initially more concentrated, a primordial origin for the observed relative spatial distributions of the FG and SG

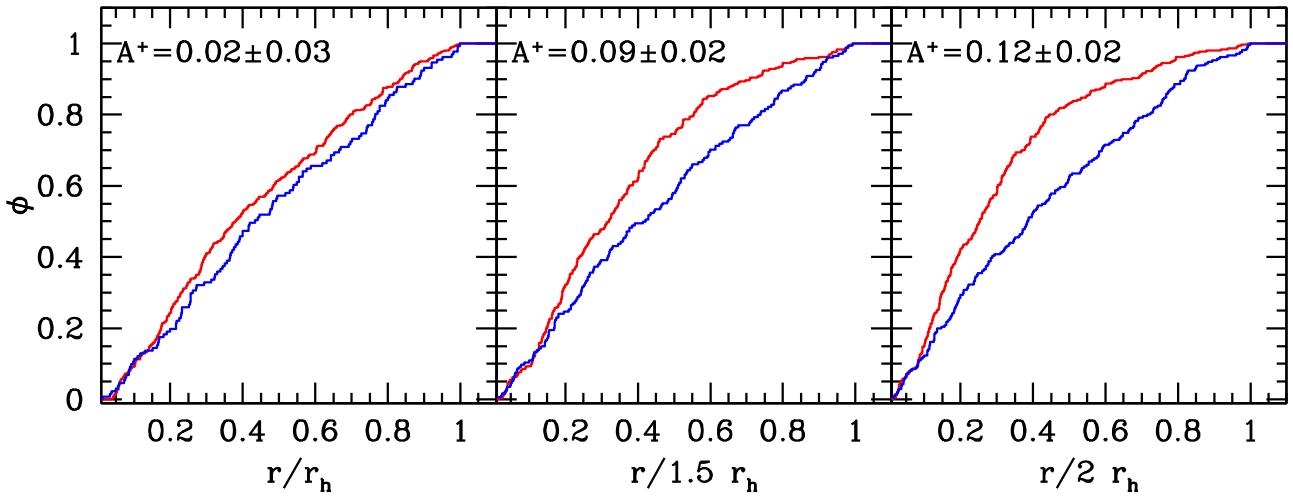

Figure 5. Cumulative radial distributions of FG (red) and SG_{EXT} (blue) stars as obtained for 1.0, 1.5, and 2.0 r_h (moving from the left to the right panel) from C_{grav}. Derived values of A^+ are reported in each panel.

populations observed in M80 seems difficult to reconcile with the cluster's long-term dynamical evolution.

We now investigate the possibility that the different radial distributions are due to a different average stellar mass of the two subpopulations. This would indeed be the case if the two populations are characterized by different helium abundances. This option was also considered by Larsen et al. (2015) to explain the inner inversion in the radial profile of the SG-to-FG number ratio found in M15. However, in that case the required mass difference was too large and inconsistent with the observations.

In Figure 6's panels (c) to (f), we show the time evolution of A^+ calculated for FG stars with masses in the range 0.80–0.85 $M_\odot$ and SG stars with two different stellar mass ranges: $0.75 \leqslant m/M_\odot \leqslant 0.80$ (panels (c) and (d)) and $0.70 \leqslant m/M_\odot \leqslant 0.75$ (panels (e) and (f)). In these two cases the difference between the mean mass of FG stars and that of SG stars is, respectively, equal to about 0.05 $M_\odot$ and 0.1 $M_\odot$. These mass differences correspond to an enhancement in the helium abundance of SG stars of $\Delta Y \sim 0.05$–0.06 (see Section 6).

Figure 6 (panels (c) to (f)) clearly demonstrates that when SG stars are assumed to be slightly less massive than FG stars, A^+ evolves toward positive values corresponding to a configuration in which the less massive SG stars are less concentrated than the more massive FG stars. Even the small mass difference we considered in our simulations is sufficient to significantly shift the values reached by A^+ late in the cluster evolution toward positive values. Such an effect brings the simulations in good agreement with the observational values of A^+ for M80. As a consequence, a different average mass between FG and SG_{EXT} stars appears to be a viable solution to reproduce the unexpected radial distribution in this system.

Another possible explanation was proposed by Hénault-Brunet et al. (2015), who suggested that the preferential disruption of SG binaries (see, e.g., Vesperini et al. 2011; Hong et al. 2015, 2016) might lead to the higher central concentration of FG stars relative to SG stars observed in the central regions. No models or simulations were carried out in Hénault-Brunet et al. (2015) to test this hypothesis, and it is unclear whether this is actually a viable option.

The solution based on mass differences seems to be dynamically robust. However, we note that this possibility should be further tested by additional studies of the spatial distributions in clusters with extreme populations characterized by non-negligible differences in helium. As shown by our simulations, however, also in these cases a cluster needs to be dynamically old before the dynamical consequences of differences in mass manifest themselves in the spatial distribution of the two populations. Moreover the extent of this effect may also depend on the radial coverage of the observational data used to calculate the A^+ parameter.

6. Observational Constraints on He Abundance Variations

In this section we investigate whether the average He (mass) difference between LE-MPs inferred from the dynamical study (Section 5) is compatible with He-abundance-sensitive photometric features in the CMD. To this aim we use a proper comparison between theoretical models and the observed morphology of the HB.

To constrain the He spread necessary to match the observed HB morphology of M80, we employed the same approach described in detail by Dalessandro et al. (2011b, 2013), which is based on a comparison between synthetic HB calculations and UV-optical CMDs. For the redder (cooler) portion of the HB, this comparison is performed with stars within the black box in the (m_{F336W}, $m_{F336W} - m_{F555W}$) CMD (Figure 7, upper panel), while for bluer stars we take advantage of the reduced bolometric corrections at UV bands using stars located within the box in the (m_{F160BW}, $m_{F160BW} - m_{F555W}$) diagram (Figure 7, lower panel). In both boxes stars are distributed almost horizontally in the corresponding CMDs. As a consequence, in these regions the effect of He variations is more pronounced.

Our HB simulations require the specification of four parameters: the minimum value of Y (Y_{min}, fixed to $Y = 0.246$), the range of He abundances (ΔY), the mean value of the mass lost along the RGB (ΔM), and the spread around it ($\sigma(\Delta M)$). Our synthetic HB code first randomly draws a value of Y (we assume for simplicity a uniform probability distribution) and determines the initial mass of a star at the RGB tip (M_{TRGB}) from interpolation among a set of BaSTI α-enhanced HB tracks and isochrones (Pietrinferni et al. 2006) with [Fe/H] $= -1.62$, and an age of 12 Gyr. The mass of the corresponding object evolving along the HB (M_{HB}) is then given by $M_{HB} = M_{TRGB} - \Delta M$, plus a random Gaussian

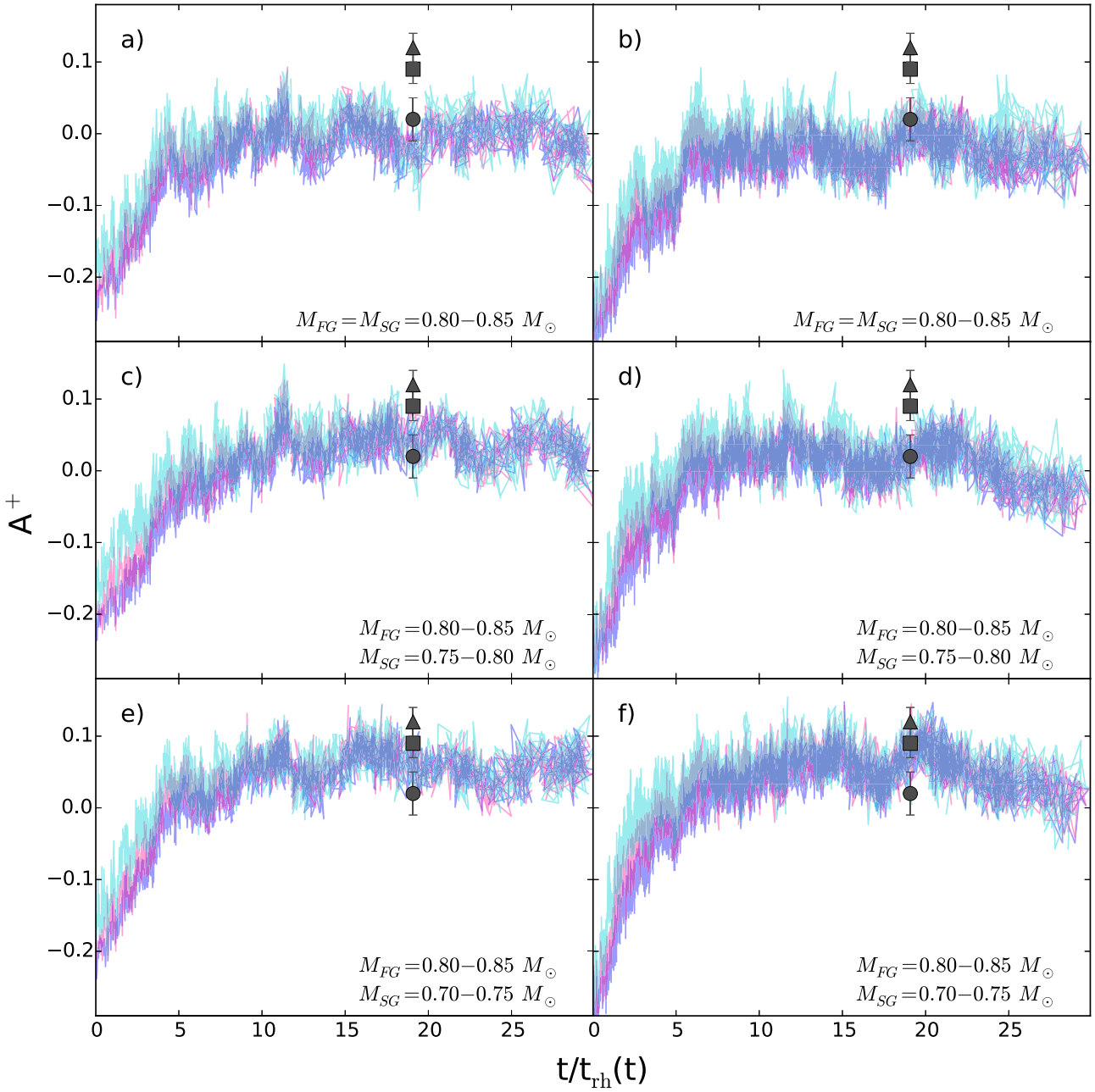

Figure 6. Time evolution of the A^+ parameter for the simulations starting with $r_h^{FG} = 5 \times r_h^{SG}$, (left hand panels) and those for $r_h^{FG} = 10 \times r_h^{SG}$ (right hand panels). The two panels in the top rows ((a) and (b)) show the evolution of A^+ calculated using FG and SG stars with masses between 0.80 and 0.85 $M_\odot$. The panels in the middle row ((c) and (d)) show the evolution of A^+ calculated using FG stars with masses between 0.80 and 0.85 $M_\odot$ and SG stars with masses between 0.75 and 0.80 $M_\odot$. The panels in the bottom row ((e) and (f)) show the evolution of A^+ calculated using FG stars with masses between 0.80 and 0.85 $M_\odot$ and SG stars with masses between 0.70 and 0.75 $M_\odot$. In each panel the three lines show the time evolution of A^+ calculated within a distance from the cluster center equal to 1 (dark turquoise), 1.5 (pink), and 2 (blue) projected half-mass radii. Time is normalized to the instantaneous half-mass relaxation time. The three gray dots show the observational values calculated within 1, 1.5 and 2 (circle, square, and triangle, respectively) half-mass radii for the FG and SG subpopulations in M80 (see Section 4).,

perturbation $\sigma(\Delta M)$. The WFPC2 magnitudes of the synthetic star are then determined according to its position along the HB track with appropriate mass and Y, obtained by interpolation among the available set of HB tracks, after an evolutionary time t has been randomly extracted, assuming that stars reach the zero age horizontal branch (ZAHB) at a constant rate. We therefore employed a flat probability distribution for t ranging from zero to t_{HB}, where t_{HB} denotes the time spent from the ZAHB to the He-burning shell ignition along the early asymptotic giant branch. The value of t_{HB} is set by the mass with the longest lifetime (the lowest masses for a given Y and Z). This implies that for some synthetic object the randomly selected value of t will be longer than its t_{HB}, or, in other words, that they have already evolved to the next evolutionary stages. The derived synthetic magnitudes are finally perturbed with a Gaussian 1σ error determined from the data quality and reduction procedures. As done by Dalessandro et al. (2011b, 2013), we mimicked the effect of radiative levitation by applying bolometric corrections appropriate for a [Fe/H] = 0.0 and scaled-solar mixture when the effective temperature is

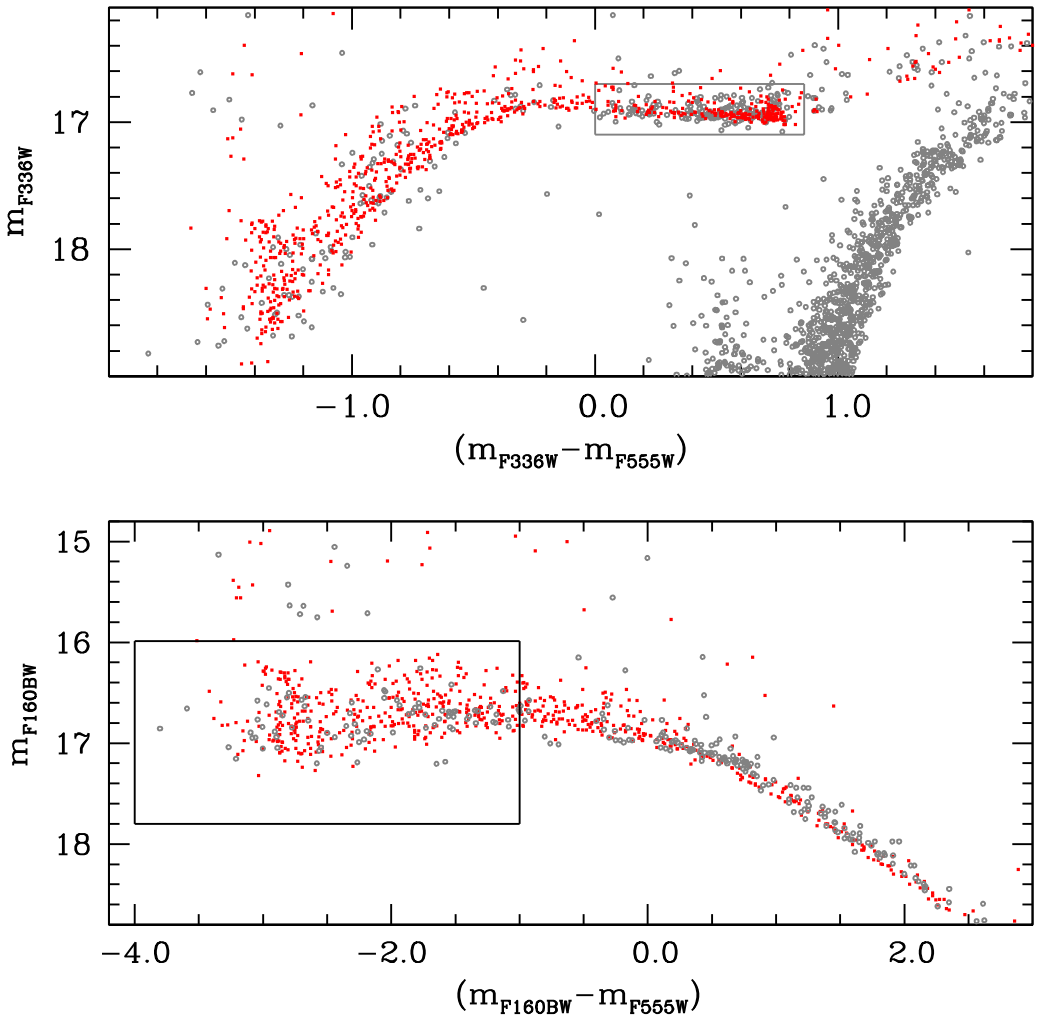

Figure 7. Observed (m_{F336W}, $m_{F336W} - m_{F555W}$) and (m_{F160BW}, $m_{F160BW} - m_{F555W}$) CMDs (upper and bottom panels, respectively) of the HB stars of M80 (black open circles). The black boxes define the red part of the HB (upper panel) and the blue one (bottom panel) where the HB analysis has been performed. The best-fitting synthetic HBs (red points) are overplotted for comparison.

larger than 12,000 K. Bolometric corrections and extinction effects have been calculated as in Dalessandro et al. (2011b).

We adopted an average reddening of $E(B - V) = 0.18$ (see the 2010 version of the Harris globular cluster catalog—Harris 1996). We then performed hundreds of HB simulations[11] by varying the distance modulus and exploring adequate ranges of ΔY, ΔM, and $\sigma(\Delta M)$ to reproduce both the lower envelope—defined as the faintest magnitude bin where the star counts are at least 2σ above zero—of the observed magnitude distributions in both the adopted boxes (Figure 7), and the mean values (and 1σ dispersion) of the magnitudes in both boxes, with an accuracy better than 0.01 mag.

We find that the observed HB is best reproduced by a true distance modulus $(m - M)_0 = 15.14 \pm 0.05$ (which is in good agreement with the literature (see, e.g., Harris 1996)) a maximum He variation $\Delta Y = 0.055$, a mass-loss law given by $\Delta M = 0.170 + 2 \times (Y - 0.246)$ and a Gaussian spread $\sigma(\Delta M) = 0.015$.[12] The resulting synthetic CMDs are shown in Figure 7, Figure 8 shows a comparison between the best-fit model and the observed star count distributions for the HB population, and Figure 9 shows the derived distribution of Y as a function of the ($m_{F336W} - m_{F555W}$) and ($m_{F160BW} - m_{F555W}$) colors.

This analysis demonstrates that a range of He abundance reaching $\Delta Y = 0.05$–0.06 is needed to reproduce the HB morphology of M80 and its magnitude is in very good agreement with that obtained using dynamical constraints (see Section 5). We warn the reader that the exact values of the derived He abundances are subject to uncertainties, mainly because of the assumptions made to simulate the effect of radiative levitation. However, we have verified that even assuming bolometric corrections appropriate for [Fe/H] = +0.5 to mimic radiative levitation, the quoted results change by $\Delta Y < 0.01$. With this caveat in mind, it is interesting to note that Figure 9 shows that a significant fraction of HB stars have $Y > 0.28$–0.29, consistent with the number of SG stars observed along the RGB. This observational result provides independent support to the interpretation of the LE-MP relative radial distribution provided in Section 5 and based on the average mass difference between FG and SG_{EXT} stars.

[11] The number of stars in each simulation is much higher than the observed sample, to reduce the effect of statistical number fluctuations on the synthetic HB.

[12] The required total RGB mass-loss ΔM increases with increasing Y. A ΔM constant with varying Y would not be able to cover the full observed color ranges for the range of Y that matches the observed magnitude distributions.

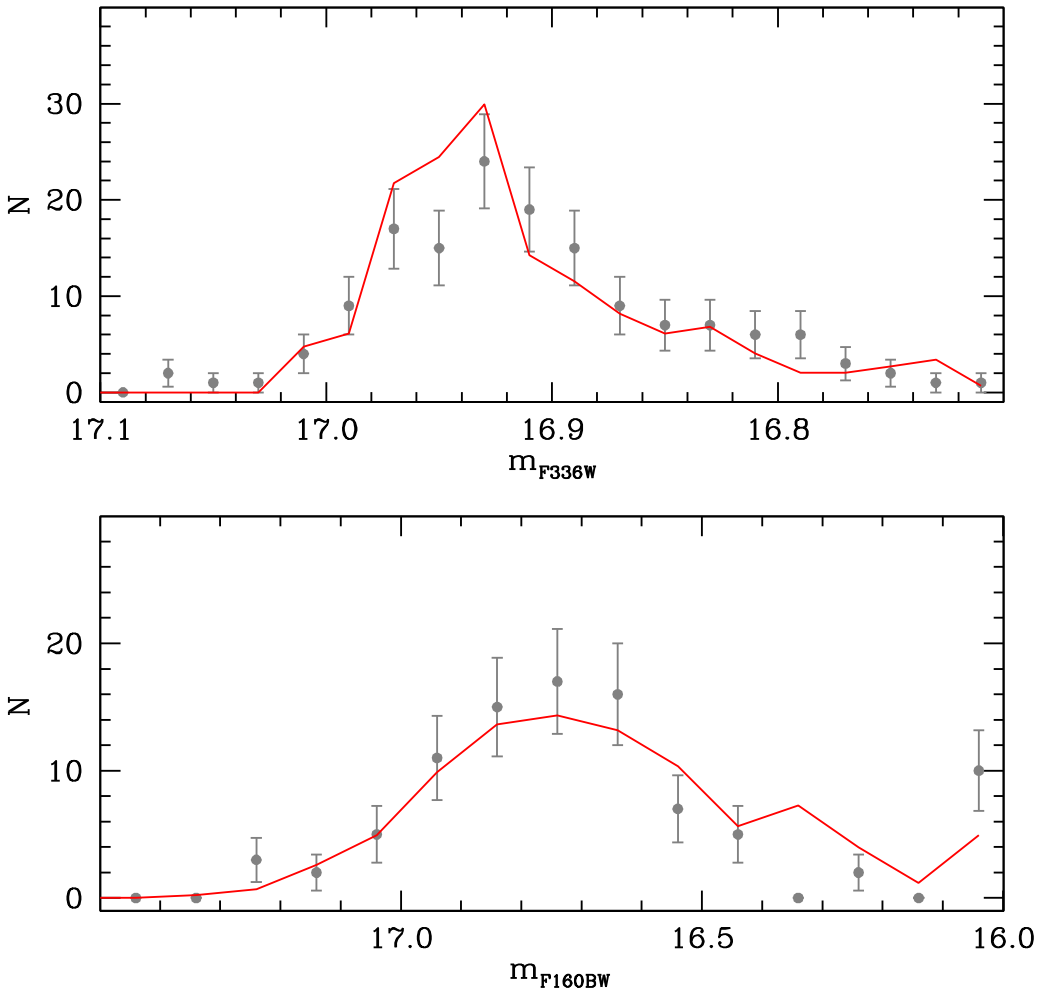

Figure 8. Comparison between observed (gray points) and theoretical best-fit (red line) star counts for the HB population, as a function of m_{F336W} and m_{F160BW} magnitudes.

7. Summary and Conclusions

We have combined *HST* optical and near-UV images to study the radial distribution of the LE-MPs in the massive globular cluster M80 out to $\sim 2.5 \times r_h$. At least three subpopulations differing in terms of light-element abundances can be clearly identified along the cluster's RGB. Surprisingly, we find that FG stars are significantly more centrally concentrated than both SG_{INT} and SG_{EXT} subpopulations for the entire radial extension covered by our data, with the difference being more significant for FG and SG_{EXT} stars.

Our puzzling findings seem to be in tension with models of formation of LE-MPs in GCs, which predict that SG stars form more centrally concentrated than FG stars, and dynamical evolution gradually erases their initial differences, eventually leading, for the most evolved clusters, to a complete spatial mixing. Indeed, this result raises a number of questions concerning the possible role of cluster formation and dynamical history in determining the observed spatial distributions of FG and SG stars.

We used the A^+ parameter (Alessandrini et al. 2016; Lanzoni et al. 2016) to provide a quantitative measure of the difference in the FG and SG spatial distributions observed in M80. This parameter, initially introduced to study the degree of segregation of BSS in globular clusters, is extremely useful for performing homogeneous and quantitative comparisons of the distributions of different types of stars with other clusters and dynamical models.

In order to shed light on the extent to which this observational result is actually an anomaly, we present the results of a set of *N*-body simulations following the time evolution of A^+ in multiple-population clusters. We find that our simulations are not able to reproduce the observed values of A^+ when assuming that FG and SG stars have the same average mass. In fact, in dynamically evolved systems like M80, simulations predict FG and SG stars to be totally mixed irrespective of their original configuration.

We have explored the possibility that the different spatial distributions are caused by different average stellar masses of the FG and SG stars. With this assumption, our *N*-body simulations are able to recover the range of observed values of A^+. In particular, we find that by assuming a small difference in the average mass of $\Delta M \sim 0.05$–$0.10\ M_\odot$ (Figure 5 panels from (c) to (f)), the observed values of A^+ are nicely reproduced. We argue that the imposed mass of the two subpopulations can result from the different evolutionary timescales of stars with a different He abundance of $\Delta Y \sim 0.05$–0.06. Interestingly, based on a detailed comparison between far-UV photometry and theoretical models, we find that such He variation is in fact needed to reproduce the observed HB morphology of the cluster. Therefore, a mass

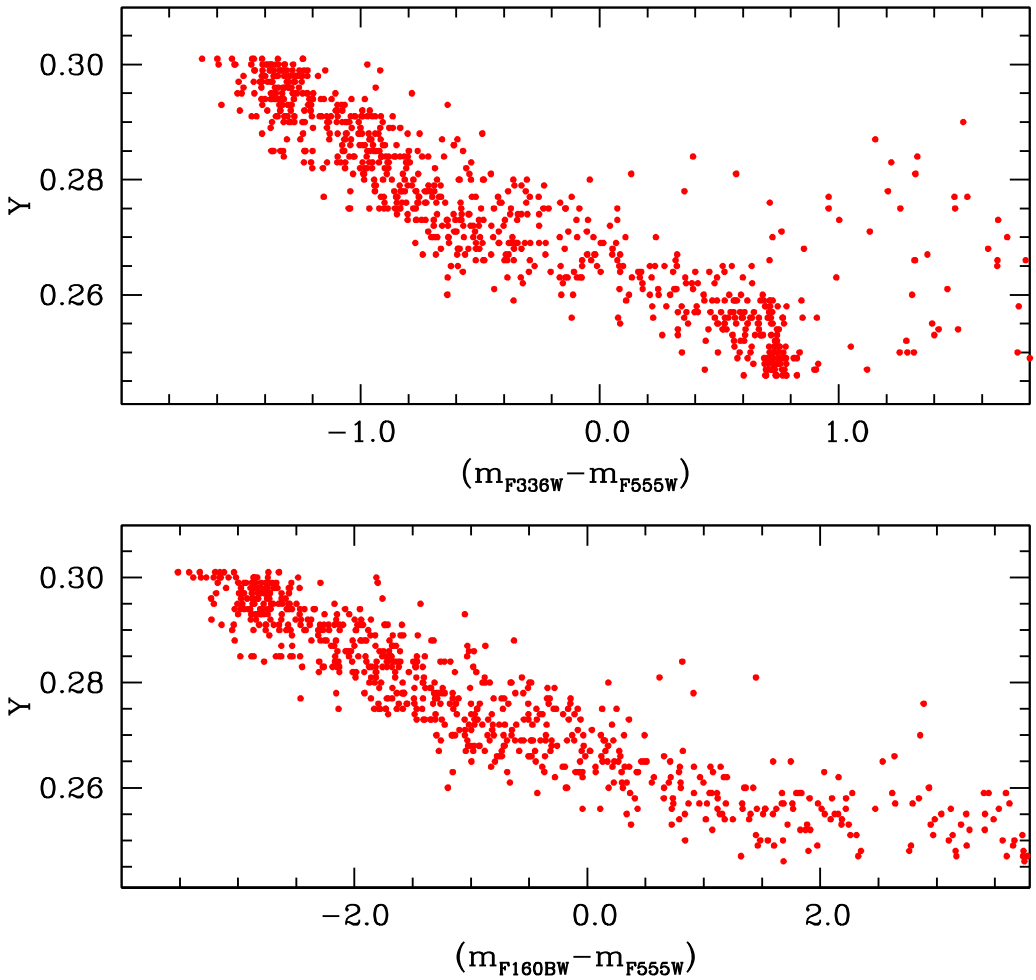

Figure 9. Y distribution as a function of the ($m_{F336W} - m_{F555W}$) and ($m_{F160BW} - m_{F555W}$) colors along the HB of M80 for the best-fitting model.

difference between the FG and the helium enriched SG populations provides a plausible and dynamically robust interpretation of our observational result.

Our analysis has shown that small differences in the average mass may play a critical role in shaping the radial distributions of LE-MPs in dynamically evolved systems and therefore they should be carefully accounted for in the interpretation of the observed radial distribution differences, in particular for dynamically evolved systems. A more extended survey of simulations covering a broader range of initial conditions would be necessary to further explore these issues and provide a more comprehensive characterization of the extent of the expected differences in the spatial distribution for different radial coverage and dynamical ages. On the observational side, additional studies aimed at exploring the spatial distributions of extreme SG populations are essential to provide additional constraints for the study of the dynamics of multiple populations and the manifestations of the possible differences in the masses of FG and SG stars.

E.D. warmly thank Peter Stetson for kindly providing ground-based photometric catalogs of M80. The authors thank the anonymous referee for the careful reading of the paper and the constructive comments.

Software: CataXcorr (P. Montegriffo—http://davide2.bo.astro.it/~paolo/Main/CataPack.html), DAOPHOT IV Stetson (1987), McLuster Küpper et al. (2011), NBODY6 Aarseth (2003); Nitadori & Aarseth (2012).

ORCID iDs

E. Dalessandro https://orcid.org/0000-0003-4237-4601
M. Cadelano https://orcid.org/0000-0002-5038-3914
F. R. Ferraro https://orcid.org/0000-0002-2165-8528
B. Lanzoni https://orcid.org/0000-0001-5613-4938
S. Raso https://orcid.org/0000-0003-4592-1236

References

Aarseth, S. J. 2003, in Gravitational N-Body Simulations, ed. J. S Aarseth (Cambridge: Cambridge Univ. Press), 430
Alessandrini, E., Lanzoni, B., Ferraro, F. R., Miocchi, P., & Vesperini, E. 2016, ApJ, 833, 252
Bellini, A., Vesperini, E., Piotto, G., et al. 2015, ApJL, 810, L13
Cadelano, M., Dalessandro, E., Ferraro, F. R., et al. 2017, ApJ, 836, 170
Chung, C., Yoon, S.-J., & Lee, Y.-W. 2011, ApJL, 740, L45
Cordero, M. J., Hénault-Brunet, V., Pilachowski, C. A., et al. 2017, MNRAS, 465, 3515
Dalessandro, E., Beccari, G., Lanzoni, B., et al. 2009, ApJS, 182, 509
Dalessandro, E., Ferraro, F. R., Massari, D., et al. 2013, ApJ, 778, 135
Dalessandro, E., Ferraro, F. R., Massari, D., et al. 2015, ApJ, 810, 40
Dalessandro, E., Lanzoni, B., Beccari, G., et al. 2011a, ApJ, 743, 11
Dalessandro, E., Lanzoni, B., Ferraro, F. R., et al. 2008, ApJ, 677, 1069
Dalessandro, E., Lapenna, E., Mucciarelli, A., et al. 2016, ApJ, 829, 77
Dalessandro, E., Massari, D., Bellazzini, M., et al. 2014, ApJL, 791, L4
Dalessandro, E., Salaris, M., Ferraro, F. R., et al. 2011b, MNRAS, 410, 694
Decressin, T., Charbonnel, C., & Meynet, G. 2007, A&A, 475, 859

de Mink, S. E., Pols, O. R., Langer, N., & Izzard, R. G. 2009, A&A, 507, L1
Denissenkov, P. A., & Hartwick, F. D. A. 2014, MNRAS, 437, L21
D'Ercole, A., Vesperini, E., D'Antona, F., McMillan, S. L. W., & Recchi, S. 2008, MNRAS, 391, 825
Dolphin, A. E. 2000, PASP, 112, 1397
Ferraro, F. R., Lanzoni, B., Dalessandro, E., et al. 2012, Natur, 492, 393
Ferraro, F. R., Paltrinieri, B., Fusi Pecci, F., Rood, R. T., & Dorman, B. 1998, ApJ, 500, 311
Ferraro, F. R., Paltrinieri, B., Rood, R. T., & Dorman, B. 1999, ApJ, 522, 983
Ferraro, F. R., Sills, A., Rood, R. T., Paltrinieri, B., & Buonanno, R. 2003, ApJ, 588, 464
Goldsbury, R., Richer, H. B., Anderson, J., et al. 2010, AJ, 140, 1830
Gratton, R. G., Carretta, E., & Bragaglia, A. 2012, A&ARv, 20, 50
Harris, W. E. 1996, AJ, 112, 1487
Hénault-Brunet, V., Gieles, M., Agertz, O., & Read, J. I. 2015, MNRAS, 450, 1164
Hong, J., Vesperini, E., Sollima, A., et al. 2015, MNRAS, 449, 629
Hong, J., Vesperini, E., Sollima, A., et al. 2016, MNRAS, 457, 4507
King, I. R. 1966, AJ, 71, 64
Kroupa, P. 2001, MNRAS, 322, 231
Küpper, A. H. W., Maschberger, T., Kroupa, P., & Baumgardt, H. 2011, MNRAS, 417, 2300
Lanzoni, B., Ferraro, F. R., Alessandrini, E., et al. 2016, ApJL, 833, L29
Lardo, C., Bellazzini, M., Pancino, E., et al. 2011, A&A, 525, A114
Larsen, S. S., Baumgardt, H., Bastian, N., et al. 2015, ApJ, 804, 71
Larsen, S. S., Brodie, J. P., Grundahl, F., & Strader, J. 2014, ApJ, 797, 15
Lim, D., Lee, Y.-W., Pasquato, M., Han, S.-I., & Roh, D.-G. 2016, ApJ, 832, 99
Lupton, R. 1993, Statistics in Theory and Practice (Princeton, NJ: Princeton Univ. Press)
Massari, D., Lapenna, E., Bragaglia, A., et al. 2016, MNRAS, 458, 4162
Mastrobuono-Battisti, A., & Perets, H. B. 2013, ApJ, 779, 85
Miholics, M., Webb, J. J., & Sills, A. 2015, MNRAS, 454, 2166
Milone, A. P., Piotto, G., Bedin, L. R., et al. 2012, A&A, 540, A16
Milone, A. P., Piotto, G., Renzini, A., et al. 2017, MNRAS, 464, 3636
Mucciarelli, A., Carretta, E., Origlia, L., & Ferraro, F. R. 2008, AJ, 136, 375
Nardiello, D., Milone, A. P., Piotto, G., et al. 2015, A&A, 573, A70
Nardiello, D., Milone, A. P., Piotto, G., et al. 2018, MNRAS, 477, 2004
Nitadori, K., & Aarseth, S. J. 2012, MNRAS, 424, 545
Pietrinferni, A., Cassisi, S., Salaris, M., & Castelli, F. 2006, ApJ, 642, 797
Piotto, G., Milone, A. P., Bedin, L. R., et al. 2015, AJ, 149, 91
Raso, S., Ferraro, F. R., Dalessandro, E., et al. 2017, ApJ, 839, 64
Richer, H. B., Heyl, J., Anderson, J., et al. 2013, ApJL, 771, L15
Savino, A., Massari, D., Bragaglia, A., Dalessandro, E., & Tolstoy, E. 2018, MNRAS, 474, 4438
Sbordone, L., Salaris, M., Weiss, A., & Cassisi, S. 2011, A&A, 534, A9
Schiavon, R. P., Caldwell, N., Conroy, C., et al. 2013, ApJL, 776, L7
Stetson, P. B. 1987, PASP, 99, 191
Stetson, P. B. 1994, PASP, 106, 250
Vesperini, E., McMillan, S. L. W., D'Antona, F., & D'Ercole, A. 2011, MNRAS, 416, 355
Vesperini, E., McMillan, S. L. W., D'Antona, F., & D'Ercole, A. 2013, MNRAS, 429, 1913